Nature and Functionality of $La_{0.58}Sr_{0.4}Co_{0.2}Fe_{0.8}O_{3-\delta}$ / $Gd_{0.2}Ce_{0.8}O_{2-\delta}$ / $Y_{0.16}Zr_{0.84}O_{2-\delta}$ Interfaces in SOFCs

Julian Szász,[1] Florian Wankmüller,[1] Virginia Wilde,[2] Heike Störmer,[2] Dagmar Gerthsen,[2] Norbert H. Menzler,[3,*] and Ellen Ivers-Tiffée[1,z]

[1] *Institute for Applied Materials (IAM-WET), Karlsruhe Institute of Technology (KIT), D-76131 Karlsruhe, Germany*
[2] *Laboratory for Electron Microscopy (LEM), Karlsruhe Institute of Technology (KIT), D-76131 Karlsruhe, Germany*
[3] *Forschungszentrum Jülich GmbH, Institute of Energy and Climate Research, Materials Synthesis and Processing (IEK-1), D-52425 Jülich, Germany*

Interdiffusion phenomena and secondary phase formation at the interface $La_{0.58}Sr_{0.4}Co_{0.2}Fe_{0.8}O_{3-\delta}$ (LSCF) / $Gd_{0.2}Ce_{0.8}O_{2-\delta}$ (GDC) / $Y_{0.16}Zr_{0.84}O_{2-\delta}$ (YSZ) are correlated to linear and non-linear losses in symmetrical and full SOFC cells. FIB/SEM (focussed ion beam / scanning electron microscopy) tomography is applied for determining the local distribution of the primary phases LSCF, GDC, and YSZ and elemental analysis via STEM/EDXS (scanning transmission electron microscopy / energy dispersive X-ray spectroscopy) provides information on the secondary phase $SrZrO_3$ (SZO) and the interdiffusion between GDC and YSZ (ID). This reveals the effect of GDC co-sintering temperature (varied from 1100°C to 1400°C), alongside the sintering of LSCF at 1080°C, on these multi-layered microstructures. Electrochemical impedance spectra on symmetrical cells show that the polarization resistance (ASR_{cat}) of the cathode/electrolyte interface is pronouncedly affected by three orders of magnitude, changing the overall power density of anode supported SOFC single cells at 0.8V by as much as a factor of 20. In conclusion, the chemical composition of the ID has a tremendous impact on the electrochemical efficiency of the investigated LSCF/GDC/YSZ interface, and processing parameters of anode supported cells with LSCF cathode have to be carefully chosen for individual SOFC cell concepts.
 [DOI: 10.1149/2.0031811jes]

Manuscript submitted June 5, 2018; revised manuscript received July 27, 2018. Published August 4, 2018.

$(La,Sr)(Co,Fe)O_{3-\delta}$ (LSCF) is the best-investigated mixed ionic-electronic (MIEC) cathode material used in solid oxide fuel cells (SOFC). The oxygen-exchange kinetics at the solid/gas interface are characterized by the surface exchange coefficient k^{δ}. Many research groups have used model samples to investigate the oxygen exchange reaction, which is highly sensitive to changes in chemical composition in the near-surface lattice.[1–5] It is a commonly accepted fact that Sr depletes from the LSCF-bulk at temperatures above 600°C, diffusing to the surface and forming SrO, or $Sr(OH)_2$ due to humidity and then evaporating into the gas phase.[6–8] Both effects are strongly adverse to surface kinetics decreasing the exchange coefficient two orders of magnitude.[9] However, there is a large scattering of both initial and final k^{δ} values in literature, which is partly caused by differences in preparation methods and the varying chemical composition of the different model samples, and also partly by different analytical methods. A screen-printed and sintered porous LSCF cathode of an anode-supported single cell and its performance degradation over 1000 h was investigated for the first time by Endler-Schuck et al.[10] The Gerischer-type impedance schematically describes (according to Adler et al.[11]) the behavior of an MIEC cathode as a coupling of the solid-state oxygen-ion transport and the oxygen surface exchange. The Endler-Schuck et al. investigation led to a clear conclusion;[10] besides the surface exchange reaction, the oxygen-ion transport in LSCF, characterized by its bulk diffusion coefficient D^{δ}, is also affected by degradation.

Much less detailed research has been devoted to the solid/solid interface between cathode, interlayer and electrolyte, shown in Fig. 1 for an anode-supported cell (ASC). Owing to interdiffusion reactions during processing (and during continuous operation), this interface has a complex chemical composition. The adjustment of sintering temperatures during the multistep fabrication process of an ASC is of great importance. At high ASC fabrication temperatures the volatile element Sr from the LSCF cathode reacts with Zr from the YSZ ($Y_{0.16}Zr_{0.84}O_{2-\delta}$) electrolyte, forming an ion-blocking $SrZrO_3$ secondary phase at the cathode/electrolyte interface.[12–14] In order to suppress this secondary phase formation, the LSCF cathode is deposited onto a chemically inert (Zr-free) interlayer, such as doped ceria (CeO_2). This ideally acts as (i) a strontium-diffusion barrier and (ii) as an ionic-conducting transfer to the YSZ solid electrolyte.[15,16] Whether this interlayer is able to completely suppress formation of $SrZrO_3$ cannot be quantitatively determined by high-resolution STEM/EDXS (scanning transmission electron microscopy/energy dispersive X-ray spectroscopy) because this method is confined to the analysis of a thin lamella (on the length scale of a few microns).[17,18] Larger volume areas can be analyzed by SIMS (secondary ion mass spectrometry), the distribution of elements is, however, averaged over the cross-sectional area which has been removed.[19] Moreover, the elemental profiles are only determined with sufficient precision in well-defined, thin-layered geometries, as in the case of thin-film model samples.[20] A large-area section from the cathode/interlayer/electrolyte interface of a technical ASC (see Fig. 1) was recently investigated by the authors by means of correlative tomography. This novel method is based on FIB/SEM (focused ion beam / scanning electron microscopy) tomography and facilitates reconstruction of the secondary phase $SrZrO_3$, as well the reconstruction of the primary phases LSCF, GDC and YSZ. To this end, two different detectors and two different acceleration voltages were used for SEM and combined with additional elemental analysis with quantitative STEM/EDXS.[21] Moreover, the interdiffusion (ID) zone between interlayer and electrolyte, the dimensions of which are temperature-dependent, could be determined and reconstructed after co-sintering, but before operation. Further growth of the $SrZrO_3$ phase can only be expected at high operating temperatures, as observed in Ref. 22 over a period of 400 h at 1000°C on an electrolyte-supported cell (ESC) by FIB/SEM tomography.

The functionality of the interlayer can be adjusted by layer thickness, porosity, and by the absence of defects.[23] The high ionic conductivity of Gd-doped ceria (GDC or 20GDC; e.g., $Gd_{0.2}Ce_{0.8}O_{2-\delta}$) makes it a good choice.[24] Dense GDC interlayers can be obtained by physical vapor deposition (PVD) [23,25] or pulsed laser deposition (PLD),[26,27] preventing any contact between the Sr-containing LSCF cathode and the Zr-containing electrolyte (YSZ). One drawback of these thin layers (usually only a few 100 nm) are the short diffusion paths for Sr and Zr species, via defects or grain boundaries, which can still lead to the formation of $SrZrO_3$ at the LSCF/GDC interface.[17,26,28] A much

*Electrochemical Society Member.
[z]E-mail: ellen.ivers@kit.edu

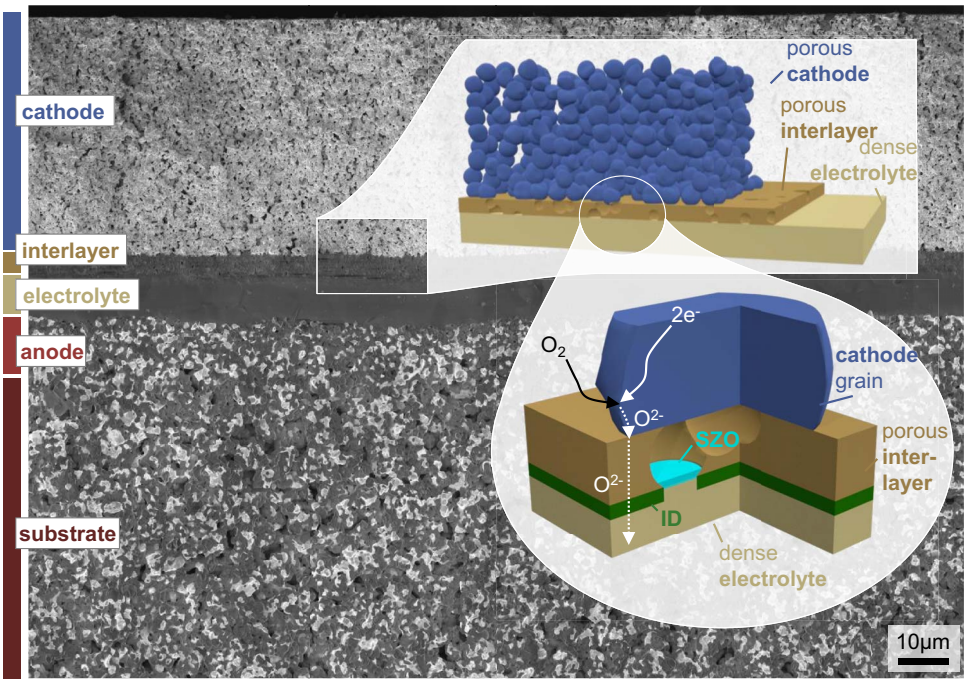

Figure 1. SEM cross-section image of an anode-supported solid oxide fuel cell with screen-printed LSCF cathode and GDC interlayer on YSZ electrolyte. Schematically magnified; the cathode/interlayer/electrolyte interface where the oxygen reduction reactions occurs and where the spatial organization of secondary phases $SrZrO_3$ (SZO) and interdiffusion of GDC and YSZ (ID) took place during the fabrication.

larger interlayer thickness is achieved using a screen-printed ASC (cf. Fig. 2, especially Fig. 2iv). The porous GDC interlayer is co-sintered and densified at high temperatures with the YSZ electrolyte (likewise screen-printed and already sintered). Owing to the high temperatures, a GDC/YSZ interdiffusion zone (green colored ID in Fig. 1) is formed between GDC and YSZ, as described above. This can decrease ionic conductivity by as much as a factor of 40 to 70.[29] Hence, co-sintering of GDC on YSZ always means a trade-off between preferably low GDC co-sintering temperatures (to minimize GDC/YSZ interdiffusion) and high GDC co-sintering temperatures (to densify the GDC interlayer and thus prevent Sr diffusion from the cathode toward the YSZ electrolyte).

The aim of the present study is to investigate the relationships between, on one hand, the co-sintering procedure of a screen-printed GDC interlayer on a YSZ electrolyte, the spatial distribution of $SrZrO_3$ and GDC/YSZ interdiffusion, and, on the other, the electrochemical performance of the resulting single cell.

Experimental

To this end, anode-supported full cells were equipped with screen-printed GDC interlayers and co-sintered at 1100, 1200, or 1300°C. Subsequently, they were provided with an LSCF cathode and then investigated by measuring their current-voltage characteristics and by applying electrochemical impedance spectroscopy (EIS). Furthermore, symmetrical cells (see Supplementary Information) were prepared in the same way, co-sintered in shorter temperature intervals up to 1400°C, and analyzed by EIS. This experimental approach is based on the well-documented fabrication routine of a state-of-the-art ASC by the Forschungszentrum Jülich whose performance and reproducibility have been frequently proven.[30] Supplementing the electrochemical measurements presented here, the same ASC's, half-cells and full cells were analyzed by high-resolution STEM, combined with EDXS for nanoscale element analysis,[31] and correlative tomography.[21] Selected findings from these studies which are essential for an understanding of the results discussed in this paper shall therefore also be presented here.

The fabrication of half-cells (anode substrate / anode functional layer / electrolyte) and further fabrication steps toward a ready-for-use full cell were carried out at Forschungszentrum Jülich, and are schematically shown in Figs. 2i–2iii.[30] The pastes used for interlayer (20GDC – $Ce_{0.8}Gd_{0.2}O_{2-\delta}$) and cathode (LSCF – $La_{0.58}Sr_{0.4}Co_{0.2}Fe_{0.8}O_{3-\delta}$) were supplied by Forschungszentrum Jülich and then applied at KIT. In order to ensure reproducibility, work was carried out in a clean-room facility, using an automated screen-printing machine, and controlled drying and sintering conditions in a script-driven furnace. GDC was screen-printed onto the electrolyte (YSZ – $Y_{0.16}Zr_{0.84}O_{2-\delta}$), dried for 24 h at 70°C, and then co-sintered either at 1100, 1200, or 1300°C, for 3 h, resulting in three different cell variants. The densification of the porous GDC interlayer is not isotropic, as its sintering is constrained by the shrinkage behavior of the half-cell. The screen-printed LSCF cathode had an active electrode area of 10 × 10 mm^2 and a thickness of 32 ± 4µm in order to ensure both ideal current distribution and homogeneous measurement conditions. LSCF was sintered for 3 h at 1080°C. Symmetrical cells (LSCF / GDC / YSZ electrolyte substrate / GDC / LSCF) were prepared in the same way, co-sintering the GDC interlayer for 3 h either at 1100, 1150, 1200, 1250, 1300, 1350, or 1400°C, resulting in seven different cell variants. The measurement setup for the electrochemical characterization of full cells has been described in great detail in Ref. 32 and for symmetrical cells in Ref. 33.

The Supporting Information section provides more details on the fabrication process, the measurement setup and the evaluation of electrochemical impedance spectroscopy. For the full cells, 5% humidified hydrogen was feed to the anode as fuel (flow 250 ml/min) and a synthetic-air mixture of O_2 and N_2 was used as oxidant (pO_2 = 0.21 atm). For symmetrical cells the oxidant was ambient air (for setup-related reasons). To facilitate comparability of the half-cells, care was taken to ensure identical sample history with respect to measurement times (<24 h).

FIB/SEM tomography was carried out with the Everhart-Thornley and in-lens detectors and optimized microscope settings (1.3 and 4 kV acceleration voltage, Zeiss 1540XB, Carl Zeiss NTS GmbH, Oberkochen, Germany) in order to resolve the grey-value information for both the secondary phase $SrZrO_3$ and GDC/YSZ interdiffusion

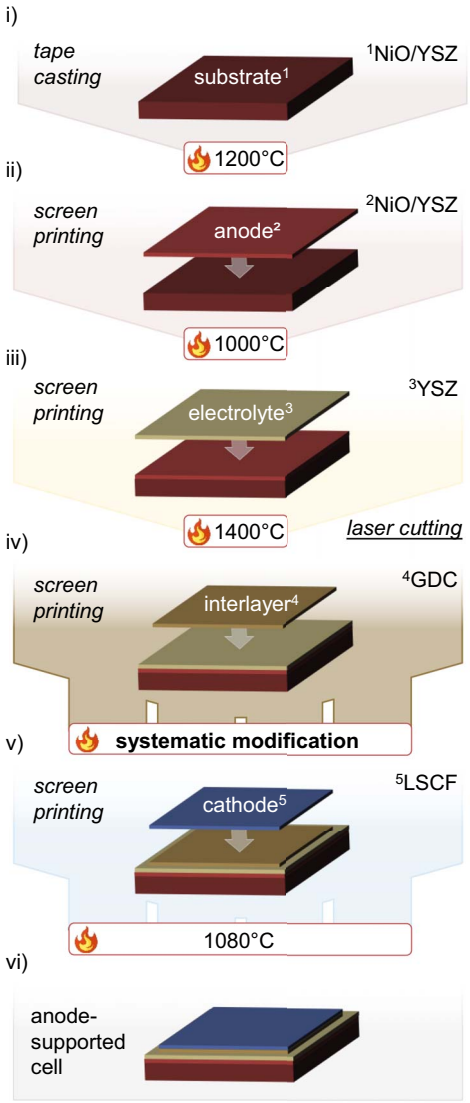

Figure 2. Fabrication routine of anode-supported fuel cells with systematic modification of the cathode/interlayer/electrolyte interface by varying the GDC co-sinter temperature in (iv) between 1100 and 1300°C in 100K.

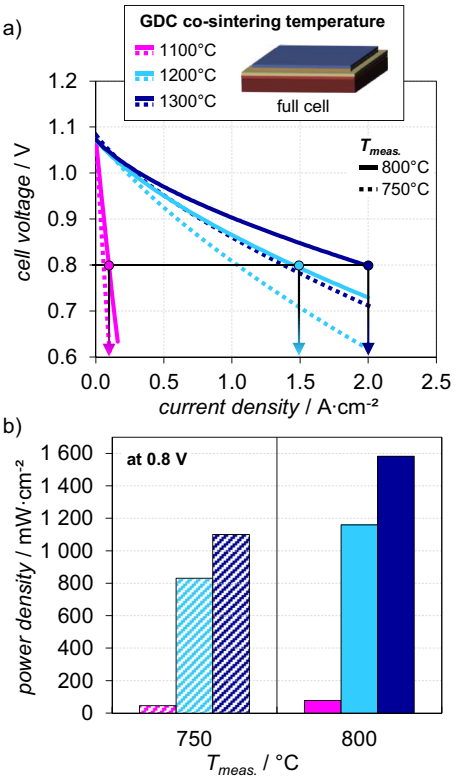

Figure 3. Performance evaluation of anode-supported cells with modified GDC co-sintering temperature, measured at $T_{meas.}$ = 750 and 800°C in syn. air (pO_2 = 0.21atm) at the cathode and 5.5.% humidified H_2 at the anode; (a) current-voltage curves and corresponding (b) power density at 0.8.V.

zone.[21] Prior to the tomography, the samples were prepared by vacuum infiltration step of a two component epoxy resin, to allow a better planar sectioning (more details about the preparation can be found in Ref. 34). The segmentation and reconstruction of the primary phases YSZ, GDC, and LSCF, as well as microstructure quantification follow the procedure described by Joos et al. in Ref. 34. Details on the STEM/EDXS analysis (FEI Tecnai Osiris ChemiSTEM and Bruker Quantax system with XFlash detector) can be found in Ref. 31.

Results

Performance evaluation of full cells.—The current-voltage characteristics of the full cells show the positive impact of an elevated GDC co-sintering temperature on the power density: at the measurement temperature of $T_{meas.}$ = 750°C the power density at 0.8 V increases from 46 mW·cm^{-2} to 831 mW·cm^{-2} and finally 1101 mW·cm^{-2}, as co-sintering temperature increases from 1100°C to 1200°C and finally 1300°C, respectively (cf. Figs. 3a and 3b). At $T_{meas.}$ = 800°C, an increase can be observed from 77 mW·cm^{-2} to 1159 mW·cm^{-2} and finally even 1582 mW·cm^{-2}.

This corresponds to a dramatic performance increase of around 1800% at a GDC co-sintering temperature of 1200°C and another 140% for a GDC co-sintering temperature of 1300°C. These measurements were carried out on state-of-the-art, full cells. This type is widely used, and have been operated for several tens of thousands of hours in SOFC stacks.[35] The measurements convincingly demonstrate the importance of correct choice of GDC co-sintering temperature for performance optimization. In the following sections, only the components forming the interface cathode/electrolyte are investigated as symmetrical cells consisting of LSCF/GDC/YSZ/GDC/LSCF. Using this setup, even co-sintering temperatures above 1300°C become accessible. In this way one can rule out any unintentional, adverse influences on the co-sintered anode performance. This is because when GDC is co-sintered above 1300°C onto an electrolyte/anode half-cell, the Ni/YSZ anode functional layer may undergo microstructural and/or chemical changes (cf. Fig. 2iii). Examples of such changes include; the reduction of the electrochemically active triple-phase boundary length between Ni, YSZ, and pores, and/or a decrease of the YSZ ionic conductivity in anode functional layer and electrolyte owing to increased tetragonal precipitation. NiO diffusion in YSZ at 1400°C and subsequent reducing conditions in the fuel gas atmosphere lead to the occurrence of tetragonal precipitates in the cubic YSZ matrix.[36–38] Hence, it would not be possible to use full cells to unambiguously attribute the performance change to the cathode/electrolyte interface.

Microstructure analysis.—We investigated the cathode/electrolyte interface of all symmetrical cells after GDC/YSZ co-sintering at 1100, 1200, 1300 and 1400°C with and without subsequent sintering of the LSCF cathode. The microstructure and the spatial configuration of primary and secondary phases, as well as of the GDC/YSZ interdiffusion, were analyzed by FIB/SEM, and for 1100 and 1400°C additionally the chemical composition by STEM/EDXS.

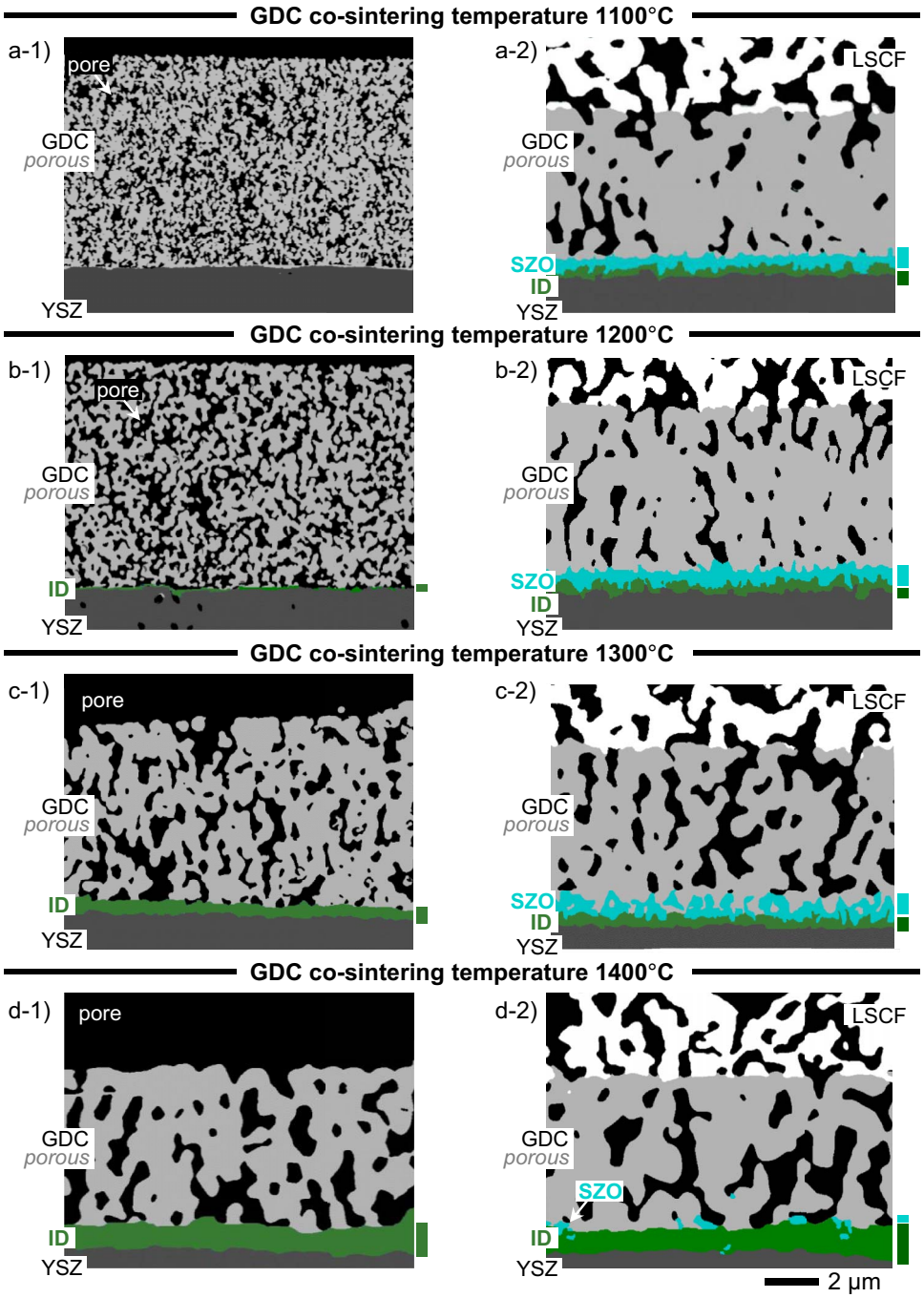

Figure 4. FIB/SEM reconstructed interfaces combined with elemental information from STEM/EDXS mappings including primary phases and the secondary phases SZO (turquoise) and ID (green). Left column (a-1), (b-1), (c-1) and (d-1): the GDC/(ID)/YSZ interface after sintering at 1100, 1200, 1300 and 1400°C respectively. Right column (a-2), (b-2), (c-2) and (d-2): the LSCF/GDC/(SZO+ID)/YSZ interface after sintering at 1080°C.

The left-hand column in Fig. 4 shows the co-sintered GDC (grey) on the YSZ electrolyte (dark-grey). Higher co-sintering temperatures expectedly lead to grain growth and shrinkage of the GDC interlayer. GDC/YSZ interdiffusion (green) can be detected starting from 1200°C (see Fig. 4b-1) and increasing up to a thickness of approx. 1.10 µm at a co-sintering temperature of 1400°C. GDC interlayer thickness is 7.7 µm at 1100°C and decreases to 6.1 µm at a GDC co-sintering temperature of 1400°C (cf. Fig. 5a). Surprisingly, the relative density of the different GDC interlayers (Fig. 5b), determined from tomography data, remains almost constant at 65% (or 35% porosity). This indicates a mass transport of Ce and Gd atoms in the ID zone when the sintering temperature increases. Note that Ce and Gd in the ID zone are consequently assigned to the ID phase and are no longer considered as GDC phase when the relative density is calculated. Sub-micron GDC grains and pores (in black) exist at 1100°C, then both become larger with increased co-sintering temperature. Surprisingly, the pore volumes seem to remain interconnected in all GDC interlayers, thus maintaining an open-porous network. It was already shown by 3D FIB/SEM tomography that even after co-sintering at 1400°C the GDC interlayer (cf. Fig. 4d-1) is connected with the gas phase.[39]

The right-hand column in Fig. 4 shows the LSCF/GDC/(SZO+ID)/YSZ interfaces. The LSCF-cathode sections (white) in the upper part of each image reveal no microstructural variations. By

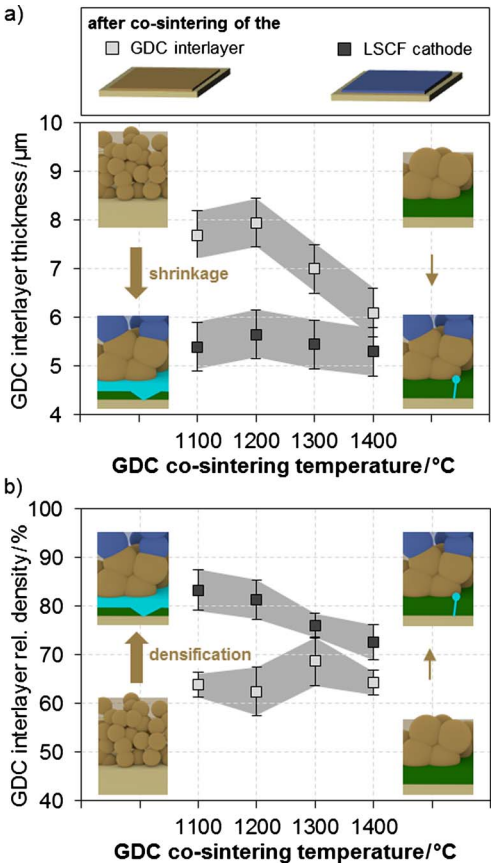

Figure 5. Development of the GDC interlayer microstructure parameters; (grey squares) after co-sintering the GDC interlayer on the YSZ electrolyte and (dark squares) after additional sintering the LSCF cathode. (a) Thickness and (b) relative density of the GDC interlayer.

evaluation of tomography data from a larger image area (>10 µm × 20 µm), a mean porosity of 40% was determined. Additional SEM fracture images reveal a cathode thickness of 32 ± 4 µm.

Unexpectedly, a post-sintering effect could be observed in the underlying GDC interlayer, when co-sintered at higher temperatures. This effect is surprisingly pronounced for the originally fine-grained and fine-porous GDC interlayer in Figs. 4a-1 and 4b-1 which was co-sintered with the YSZ electrolyte at 1100°C and 1200°C, after the subsequent sintering of the LSCF cathode at 1080°C, cf. Figs. 4a-2 and 4b-2. For a GDC co-sintering temperature of 1100°C the GDC interlayer shrinks by about 30% down to 5.4 µm and is densified by 30% to a relative density of 82% (Figs. 5a and 5b). By a quantitative evaluation of 2D and 3D image data, this post-sintering effect is also demonstrated in the case of symmetrical cells co-sintered at 1300°C and 1400°C. For a GDC co-sintering temperature of 1400°C the GDC interlayer shrinks by 13% down to 5.3 µm and is densified by 13% to a relative density of 72% (Figs. 5a and 5b). The indicated error bars for the relative density have been estimated as ± 5% for 2D FIB/SEM image data and ± 2.5% for 3D FIB/SEM tomography data.

We suppose, that this post-sintering effect is caused by the activity of gaseous LSCF cations present in the pore volume, as reported for Co, Fe and Sr in Refs. 6, 40. A further notable change after LSCF sintering at 1080°C is the appearance of an ID in symmetrical cells previously co-sintered at 1100°C and an increase of ID thickness in samples co-sintered at 1200°C. Both aspects will be discussed in the last section. The question remains, if and where the strontium species can come into contact with zirconium from the YSZ electrolyte during sintering and thus form the secondary phase $SrZrO_3$. The $SrZrO_3$ phase analyzed by STEM/EDXS is marked in turquoise in Figs. 4a-2 through 4d-2. It is obvious that its spatial distribution varies and the amount of $SrZrO_3$ decreases with increasing GDC co-sintering temperature. At GDC co-sintering temperatures of both 1100°C and 1200°C, $SrZrO_3$ forms a continuous layer with an undulating boundary both toward the bottom interdiffusion zone and the top cathode layer. This wavelike shape is more pronounced at 1300°C, and the SZO layer appears to be partially interrupted. Our group used 3D tomography to show that the 2D micrographs shown here are representative images and that the SZO layer starts to become discontinuous at 1300°C GDC co-sintering temperature.[21] At 1400°C the $SrZrO_3$ is only present in the form of isolated islands.

Material analysis.—The chemical changes caused by thermal treatment of the symmetrical cells were analyzed by STEM/EDXS. In Refs. 31, 39 we presented first reports on the underlying comprehensive STEM/EDXS study (excerpts from which shall be presented here).

After co-sintering the GDC/YSZ interface the composition of the ID zone was initially investigated using EDXS concentration profiles and element mappings. At a GDC co-sintering temperature of 1100°C the concentration profiles of Gd and Ce, as well as of Zr and Y, are clearly spatially separated, thus not leading to any significant interdiffusion phenomena at the interface (Fig. 6a-1). At 1400°C, however, a pronounced interdiffusion between GDC and YSZ occurred with an extent of approx. 1.10 µm (Fig. 6b-1), as indicated by the green markings in Fig. 4. The part of the GDC/YSZ interdiffusion zone that is in contact with the pores exhibits a dense, Ce-rich structure with a Gd dopant concentration similar to that of the utilized 20GDC. A strong blending of Ce, Zr, Gd and Y is observed in a transitional zone. This blend is effectively a solid solution with a $GDC_{0.5}YSZ_{0.5}$ composition on a width <100 nm. The part in contact with the YSZ electrolyte consists of a Zr-rich phase with a stoichiometry similar to the utilized YSZ.

After the supplementary sintering of the LSCF cathode, a local $SrZrO_3$ distribution at the GDC/YSZ interface appears in the STEM/EDXS elemental maps, similar to the results shown in Fig. 4.

At a GDC co-sintering temperature of 1100°C, a continuous SZO layer is formed (Fig. 6a-2), whereas at 1400°C the SZO only forms occasionally along ID grain boundaries and in the pores (Fig. 6b-2). This finding closely echoes SIMS analyses on thin-film model samples in Ref. 41. All samples showed an inhomogeneous dopant distribution of La (max. 8 at%), Fe (max. 11 at%), and Gd (max. 3 at%), could be detected in the $SrZrO_3$.[21,42] The STEM/EDXS results make it very clear (Fig. 6a-2) that the formation of $SrZrO_3$ is accompanied by a thin ID layer, which only forms due to the sintering of the LSCF cathode. This thin ID layer contains an increased amount of Gd (9 at%) and Y (20 at%), but only small amounts of Ce (< 3 at%), thus clearly differing chemically from the extended GDC/YSZ interdiffusion layer discussed above, which formed during GDC/YSZ co-sintering at 1400°C (cf. Fig. 6a-2 and 6b-2).

Moreover, substantial chemical changes were observed within the GDC layer itself. The results have already been described in Ref. 43 and reveal double-oxide ($FeGdO_3$) and oxide (CoO) formation, as well as a corresponding decrease of the Gd dopant concentration in the original 20GDC.[44,45] It should be explicitly noted that no Co enrichment at the GDC grain boundaries could be observed (within the measuring accuracy) in any of the areas analyzed.[43]

The LSCF/GDC interface was investigated by STEM/EDXS, too, without detecting any significant chemical changes. Only a very small amount of Gd could be found inside the LSCF, however, very close to the resolution limit (≤3 at%).[43] This can be understood given the low LSCF sintering temperature of 1080°C, because a mutual diffusion of all cations was found by Li et al. only at much higher LSCF sintering temperatures (1400°C).[46] It was shown on as-prepared symmetrical cells that the electrochemical characterization does not give rise to any chemical changes.[31]

Electrochemical characterization of symmetrical cells.—As already explained, symmetrical cells were chosen in order to avoid any cross-influences from the anode half-cell in the impedance

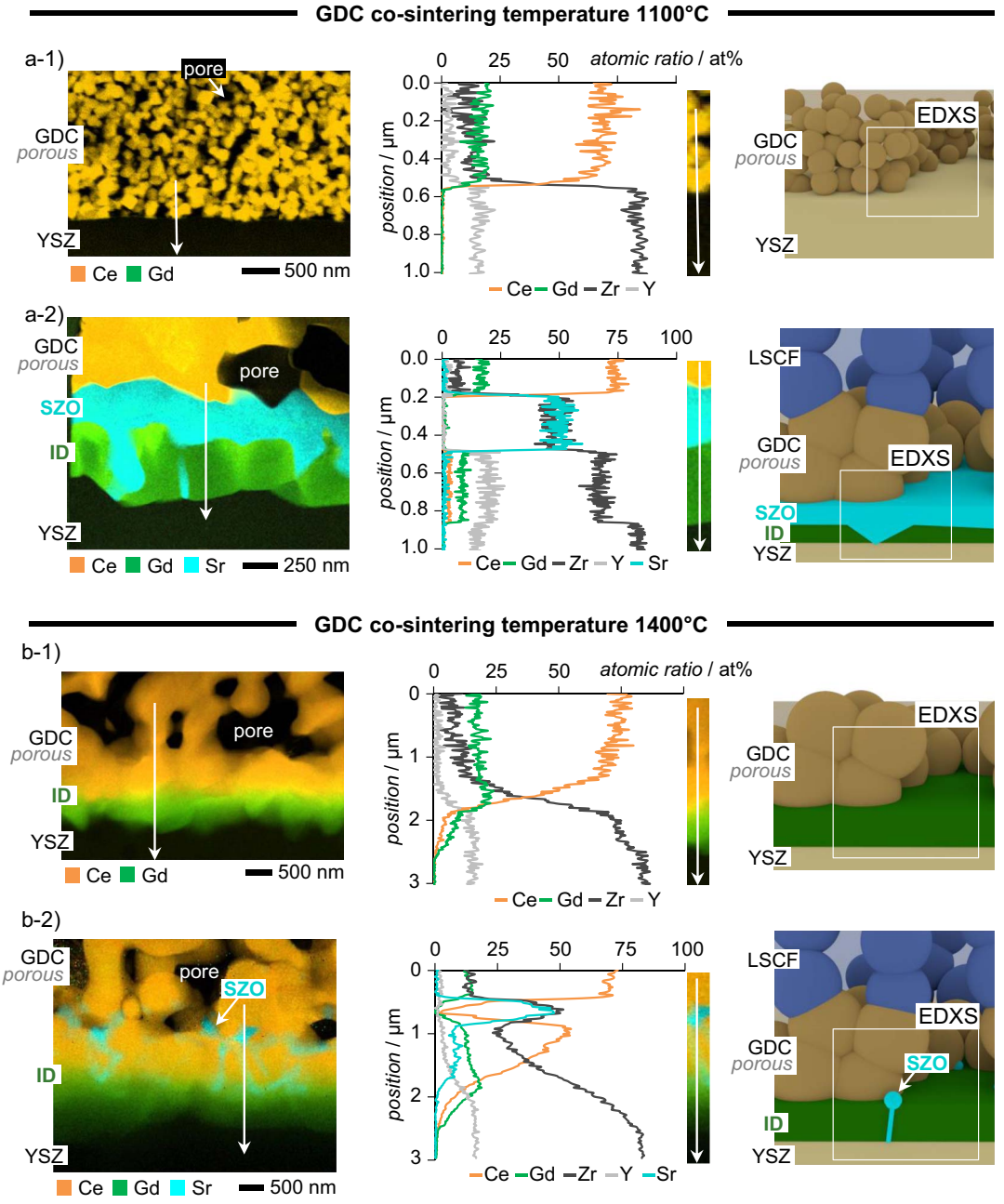

Figure 6. Interface characteristics showing the fundamental material interactions, including secondary phase formation (f.l.t.r.): STEM/EDXS-mapping, -concentration profile and schematic drawing: (a) GDC co-sintered at 1100°C: (a-1) after GDC/YSZ co-sintering and (a-2) after LSCF sintering. (b) GDC co-sintered at 1400°C: (b-1) after GDC/YSZ co-sintering and (b-2) after LSCF sintering.

spectrum. The area specific resistances of the cathode polarization (ASR_{cat}) and of the ohmic losses (ASR_{Ω}) are direct measures of the interface performance. Both quantities are determined by evaluating the electrochemical impedance spectroscopy (EIS) measurements described in detail in the Supporting Information.

Fig. 7a depicts the ASR_{cat} determined from symmetrical cells, where GDC/YSZ is co-sintered in 50 K intervals from 1100 to 1400°C, at measurement temperatures ranging from 600–800°C. Interestingly enough, ASR_{cat} values vary by three orders of magnitude, ranging from 5.329 $\Omega \cdot cm^2$ (for the co-sintering temperature 1100°C), to a maximum of 6.774 $\Omega \cdot cm^2$ (for the co-sintering temperature of 1150°C) down to 0.007 $\Omega \cdot cm^2$ (for the co-sintering temperature of 1400°C) at $T_{meas.} = 800$°C. The change in activation energy (E_{act}) from 1.43 eV (for GDC co-sintered at 1400°C) to 1.22 eV (for GDC co-sintered at 1100°C) indicates a change from the oxygen reduction reaction (with 1.3 to 1.39 eV in Refs. 32, 47) to a new rate-limiting step. This is likely to be associated with the occurrence of the secondary phase, $SrZrO_3$. The stepwise increase of co-firing temperature in 50K intervals clearly shows that co-sintering at 1100°C and 1150°C leads to the highest ASR_{cat}, while 1250°C already decreases ASR_{cat} by one order of magnitude. A rise to 1300°C has a marked impact, as it further decreases ASR_{cat} by a factor of 20. This course of ASR_{cat} became clear by finely graduating the co-firing temperatures in symmetrical cells. The trend corresponds nicely with the I/V characteristics of full cells displayed in Fig. 3. However, as this is only shown for symmetrical cells, further increasing co-sintering temperature to 1350°C or 1400°C still holds potential for improving ASR_{cat}. This result clearly indicates that GDC/YSZ co-sintering temperature has, alongside the sintering

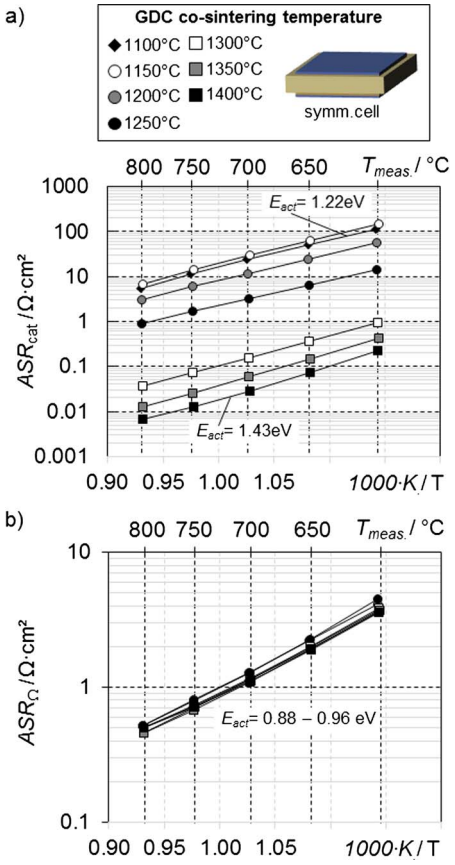

Figure 7. Area specific resistances (*ASR*) of symmetrical LSCF/GDC/YSZ-cells with modified GDC co-sintering temperature, measured in laboratory air: (a) cathode polarization resistance (ASR_{cat}), (b) ohmic resistance (ASR_{Ω}). Note that the ASR_{cat} shows half the symmetrical cell, therefore only one LSCF/GDC/YSZ interface.

temperature of LSCF, a tremendous impact on the electrochemical efficiency of the LSCF/GDC/YSZ interface, and has to be carefully chosen for individual combinations of material composition and processing routines. It also points to difficulties expected when co-firing all multilayers in a single step. For this well established multilayer system (developed by Forschungszentrum Jülich) the GDC/YSZ co-sintering should be well above 1300°C for lowest values of ASR_{cat}. Of similar importance is the ohmic loss contribution, ASR_{Ω}, depicted in Fig. 7b with an expected E_{act} between 0.88 and 0.96 eV.[24,48] It appears that the presence of SZO does not seem to have any influence on ASR_{Ω}. Given that all contacting was identical and that the YSZ electrolyte substrates and GDC interlayers of all cells are similar, any differences in ASR_{Ω} are expected to only result from the different widths and chemical compositions of the ID zone. Ergo, when considering the width, ASR_{Ω} should reach a maximum in the case of high GDC co-sintering temperatures. However, the measurements do not show any significant dependency (relative standard deviation $\leq$5%) of ASR_{Ω} on the width, therefore we suggest that the chemical composition of the ID zone must have a compensating effect.

Discussion

The results, in their entirety, show that the nature of an LSCF/GDC/YSZ interface significantly affects the electrical performance of solid oxide fuel cells. The spatial distribution of the secondary phase $SrZrO_3$, and the GDC/YSZ interdiffusion at the interface play decisive roles and are both influenced by the preparation procedure of the GDC interlayer. As the porosity of the screen-printed GDC interlayer always amounts to more than 30% (even after co-sintering with the YSZ electrolyte at 1400°C) this layer cannot prevent the formation of $SrZrO_3$. The pore networks of the GDC interlayers investigated are always interconnected to the gas phases; hence Sr activity during subsequent sintering of LSCF at 1080°C is identical for all cells. For the formation of $SrZrO_3$, however, the presence of Zr as reactant is a prerequisite, and the availability of Zr is strongly affected by the co-sintering temperature of GDC on YSZ.

At 1100°C, no GDC/YSZ interdiffusion zone is present after GDC co-sintering, and the direct contact between Sr species and YSZ leads to the formation of a dense, continuous SZO layer. The formation of $SrZrO_3$ requires the consumption of Zr at the YSZ interface, whereas Gd and Y are poorly soluble in $SrZrO_3$.[49] Hence, Gd (and very slight traces of Ce) diffuses into the YSZ and forms a 300 nm thick ID zone, yet only after subsequent sintering of the LSCF cathode. This ID zone significantly differs in its chemical composition with respect to its elevated Gd as well as Y content from the broad GDC/YSZ interdiffusion zone that forms starting at 1200°C.[39]

Matsui et al. measured the ionic conductivity of a Gd-enriched YSZ electrolyte ($ID_{Matsui} = Gd_{0.10}Y_{0.16}Zr_{0.82}O_{2-\delta}$) as $\sigma_{ion} = 0.43$ S·m^{-1} (at 800°C), which is more than 10 times lower compared to GDC (8.7 S·m^{-1}) and YSZ (5.4 S·m^{-1}).[29,50]

At 1200°C, 1300°C and 1400°C a dense interdiffusion zone is formed, which thickens with increasing co-sintering temperature and is increasingly Ce-rich and Zr-depleted toward the GDC interlayer, has a transitional zone with a $GDC_{0.5}YSZ_{0.5}$ composition, but is chemically unaltered toward the YSZ electrolyte. Tsoga et al. determined the ionic conductivity of the transitional zone after co-sintering at 1400°C ($ID_{Tsoga} = Ce_{0.37}Zr_{0.38}Gd_{0.18}Y_{0.07}O_{1.87}$) to be even lower $\sigma_{ion} = 0.125$ S·m^{-1} (at 800°C)[29].

Both compositions (ID_{Matsui} and ID_{Tsoga}) will increase the ohmic resistance, if their thickness is of relevance. However, we determined the ASR_{Ω} values of all symmetrical cells built on 200 µm thick YSZ as being identical (within the measurement accuracy), see Fig. 7b. In this study, we assume a counterbalance between ID thickness and chemical composition, as the Gd-enriched ID zone with a composition similar to ID_{Matsui} is three to four times thicker compared to the reaction product with a composition similar to ID_{Tsoga}.

Sintering of LSCF at 1080°C additionally affects the grain size, pore size, and the chemical composition of the screen-printed and co-sintered GDC interlayer. This post-sintering effect is caused by the activity of gaseous Co, Fe and Sr species, present in the pore volume. It has already been shown by other groups that the addition of Co to the GDC screen-printing paste drastically improves its shrinkage behavior [23,51] and that a dense LSCF pellet placed 1 mm away densifies a porous GDC interlayer within 50 h at 1200°C.[6] In this study we show that this effect can be observed during moderate LSCF sintering conditions (1080°C, 3h). The effect is especially pronounced in the case of small GDC grains with a large surface area, corresponding to low GDC co-sintering temperatures of 1100°C and 1200°C. Only when GDC interlayers are far thicker (>10 µm) does delamination or crack formation occur, as observed in Ref. 23. We assume that post-sintering in the GDC takes place more slowly than the formation of $SrZrO_3$, because a continuous SZO layer is able to form between GDC and (ID)/YSZ. The interaction of Co and Fe with the GDC interlayer, moreover, leads to the formation of isolated grains consisting of $FeGdO_3$ and CoO in the GDC interlayer, as previously reported by our group.[43] This results in a local redistribution of the Gd concentration within the GDC bulk, which also causes the ionic conductivity to decrease.[45] Only Co at the GDC grain boundaries would lead to an enhancement of ionic conductivity,[52] but could not be detected by means of the STEM/EDXS analysis in this study.[43] It should be stressed again, though, that the ASR_{Ω} determined on symmetrical cells does not show any measurable differences.

As the ASR_{Ω} does not change in the finely graduated symmetrical cells measured here, the different characteristics of the GDC interlayer and of the GDC/YSZ interdiffusion zone cannot have had a pronounced effect on the performance of full cells (Figs. 3a and 3b). Therefore, we ascribe the power density of full cells differing by a factor of 20 (at $T_{meas.} = 800$°C from 77 mW·cm^{-2} to 1582 mW·cm^{-2})

to the amount and spatial distribution of secondary phase $SrZrO_3$. Oxygen-ion transport starting at the LSCF cathode, moving via the GDC interlayer toward the ID zone becomes the rate-limiting factor in the case of continuous $SrZrO_3$ layers (SZO). Even the slightest gaps in the SZO layer inhibit total blockage and facilitate oxygen ion transport through the chemically modified fluorite lattice of GDC and ID to the YSZ electrolyte. This is backed by the drastic difference between the cathode polarization resistance (ASR_{cat}) at a co-sintering temperature of 1100°C (ASR_{cat} = 5.329 Ω·cm^2 at 800°C) and at 1400°C (ASR_{cat} = 0.007 Ω·cm^2 at 800°C), the difference amounting to three orders of magnitude. Particularly striking is how the correlation of the ASR_{cat} jumps in symmetrical cells by one order of magnitude with the transition of a continuous SZO layer at a GDC/YSZ co-sintering temperature of 1200°C to a discontinuous one at 1300°C. The amounts of $SrZrO_3$ still present are nevertheless able to ensure very low ASR_{cat} values of 0.037 Ω·cm^2 at 800°C. The spatially isolated distribution of $SrZrO_3$ in pores or predominately along vertically oriented ID grain boundaries is, therefore, not critical, or at least no more so than the formation of $FeGdO_3$ and CoO. The processes associated with $SrZrO_3$ (blocking of oxygen-ion transport) occur within the frequency range of cathode polarization. This suggests the existence of a high chemical capacitance and shall be addressed in detail in a subsequent paper. It can be explained by the formation of oxygen vacancies owing to the La, Fe and Gd doping of $SrZrO_3$.[53–55] On the other hand, the reason might be double-layer capacitances at the GDC/SZO or the SZO/ID interface.[49,56] Regarding the impedance of full cells, the occurrence of large amounts of $SrZrO_3$ may lead to an overlap of cathodic and anodic polarization resistances.

Besides the screen-printed and always open-porous GDC interlayer investigated here, there may of course be further parameters influencing the spatial distribution of the secondary phase $SrZrO_3$, such as

- the GDC interlayer being dense prior to subsequent sintering of the LSCF cathode,[23]
- the cathode composition itself (Sr activity),[44] and
- the chemical composition of, and impurities within, the electrolyte, to name but the most important.[57]

Therefore, as well as the results shown here, the newly developed method of secondary phase visualization in Ref. 21, the high-resolution materials analysis in Ref. 31, and model experiments in Ref. 49 are of high relevance. The results compiled by our group may ultimately serve as a basis for cell impedance modelling depending on the SZO distribution at the intricately structured cathode/electrolyte interface.

Conclusions

The performance of anode-supported SOFCs (ASCs) with an LSCF/GDC/YSZ interface on the cathode side is sensitive to a variation of processing temperatures. The chemical composition of the interdiffusion layer (and, to a lesser degree, its thickness) that forms during co-sintering of the persistently porous GDC on the YSZ electrolyte is crucial: it has a decisive influence on the amount and spatial distribution of the secondary phase $SrZrO_3$, forming during subsequent co-sintering of LSCF at lower temperatures only at sites where Zr is available as reaction partner from the YSZ electrolyte. We demonstrated how the power-density of an ASC can be changed by a factor of 20 (from 1582 mW·cm^{-2} to 77 mW·cm^{-2} at 800°C). By means of correlative tomography (FIB/SEM combined with STEM/EDXS) it could be shown that the spatial distribution of $SrZrO_3$ on symmetrical cells can be influenced by the GDC/YSZ co-sintering temperature. The porosity of the GDC layer has less influence on the formation of $SrZrO_3$ than the chemical composition of the GDC/YSZ interdiffusion zone, which depends on co-sintering temperature. If virtually no GDC/YSZ interdiffusion occurs, as is the case at low GDC sintering temperatures (1100°C), a continuous $SrZrO_3$ layer forms. As a result, Gd diffuses into the YSZ and leads to a thin interdiffusion zone. Its chemical composition (Gd- and Y-rich YSZ, absence of Ce) strongly differs from the wide GDC/YSZ interdiffusion layer formed at the very high GDC co-sintering temperatures of 1400°C. The dense SZO/ID-interface blocks the transport of oxygen ions and therefore raises the cathode polarization resistance of 0.007 Ω·cm^2 at 800°C by up to three orders of magnitude. From the results presented here it can be concluded that ideally a wide, Ce-rich and Zr-depleted ID layer should be able to effectively prevent the formation of $SrZrO_3$, even though there is a high activity of Sr due to the open porosity in the GDC layer. $SrZrO_3$ is then only occasionally formed within the pore volume or predominantly along vertically oriented ID grain boundaries, still providing sufficient diffusion pathways for oxygen ions from the ID to the YSZ. During LSCF sintering, the cations Co, Fe and Sr from the LSCF act as a sintering additive, which leads to a post-sintering of the GDC layer, densifying it by up to 30%. The GDC layers subsequently achieved relative densities of about 78 ± 5%, independent of the GDC co-sintering temperature. Therefore, less attention should be paid to the degree of compaction and the thickness of a GDC layer in post-test analyses - although the "spatial organization" of $SrZrO_3$ and GDC/YSZ interdiffusion should always be examined. The significance of these results is corroborated by the fact that ASCs fabricated with the best-suited processing parameters (co-sintering of GDC/YSZ at 1300°C, sintering of the LSCF cathode at 1080°C) have been successfully operated in many SOFC stacks (5 to 20 kW) for tens of thousands of hours. It therefore seems advisable to transfer these findings to other modifications of SOFC cells, too.

Acknowledgments

The authors sincerely thank W. Herzhof from the Forschungszentrum Jülich for the generous supply of pastes and anode-supported half-cells. Sincere thanks are given to S. Wagner for translation and J. Packham for proofreading the manuscript.

ORCID

Norbert H. Menzler https://orcid.org/0000-0001-7091-0980
Ellen Ivers-Tiffée https://orcid.org/0000-0002-8183-2460

References

1. F. Baumann, J. Fleig, H. Habermeier, and J. Maier, *Solid State Ionics*, **177**, 1071 (2006).
2. J. Druce, H. Téllez, M. Burriel, M. D. Sharp, L. J. Fawcett, S. N. Cook, D. S. McPhail, T. Ishihara, H. H. Brongersma, and J. Kilner, *Energy Environ. Sci.*, **7**, 3893 (2014).
3. N. Tsvetkov, Q. Lu, and B. Yildiz, *Faraday Discuss.*, **182**, 257 (2015).
4. M. Prestat, J.-F. Koenig, and L. J. Gauckler, *J. Electroceramics*, **18**, 87 (2007).
5. L. Wang, R. Merkle, Y. A. Mastrikov, E. A. Kotomin, and J. Maier, *J. Mater. Res.*, **27**, 2000 (2012).
6. Z. Lu, S. Darvish, J. Hardy, J. Templeton, J. Stevenson, and Y. Zhong, *J. Electrochem. Soc.*, **164**, F3097 (2017).
7. E. Bucher and W. Sitte, *Solid State Ionics*, **192**, 480 (2011).
8. X. Yin, L. Bencze, V. Motalov, R. Spatschek, and L. Singheiser, *Int. J. Appl. Ceram. Technol.*, **2**, 17 (2017).
9. E. Bucher, W. Sitte, F. Klauser, and E. Bertel, *Solid State Ionics*, **191**, 61 (2011).
10. C. Endler-Schuck, J. Joos, C. Niedrig, A. Weber, and E. Ivers-Tiffée, *Solid State Ionics*, **269**, 67 (2015).
11. S. B. Adler, J. A. Lane, and B. C. H. Steele, *J. Electrochem. Soc.*, **143**, 3554 (1996).
12. H. Yokokawa, *Solid State Ionics*, **40-41**, 398 (1990).
13. H. Yokokawa, N. Sakai, T. Kawada, and M. Dokiya, *Solid State Ionics*, **52**, 43 (1992).
14. F. W. Poulsen and N. van der Puil, *Solid State Ionics*, **53–56**, 777 (1992).
15. M. Gödickemeier and L. J. Gauckler, *J. Electrochem. Soc.*, **145**, 414 (1998).
16. H. Uchida, S. Arisaka, and M. Watanabe, *Electrochem. Solid-State Lett.*, **2**, 428 (1999).
17. S. Sønderby, P. L. Popa, J. Lu, B. H. Christensen, K. P. Almtoft, L. P. Nielsen, and P. Eklund, *Adv. Energy Mater.*, **3**, 923 (2013).
18. S. Uhlenbruck, T. Moskalewicz, N. Jordan, H.-J. Penkalla, and H. P. Buchkremer, *Solid State Ionics*, **180**, 418 (2009).
19. T. Horita, M. Nishi, T. Shimonosono, H. Kishimoto, K. Yamaji, M. E. Brito, and H. Yokokawa, *Solid State Ionics*, **262**, 398 (2014).
20. J. C. De Vero, K. Develos-Bagarinao, H. Kishimoto, T. Ishiyama, K. Yamaji, T. Horita, and H. Yokokawa, *J. Electrochem. Soc.*, **163**, 1463 (2016).

21. F. Wankmüller, J. Szász, J. Joos, V. Wilde, H. Störmer, D. Gerthsen, and E. Ivers-Tiffée, *J. Power Sources*, **360**, 399 (2017).
22. T. Matsui, M. Komoto, H. Muroyama, K. Kishida, H. Inui, and K. Eguchi, *J. Power Sources*, **312**, 80 (2016).
23. A. Mai, V. Haanappel, F. Tietz, and D. Stöver, *Solid State Ionics*, **177**, 2103 (2006).
24. Z. Tianshu, P. Hing, H. Huang, and J. Kilner, *Solid State Ionics*, **148**, 567 (2002).
25. F. C. Fonseca, S. Uhlenbruck, R. Nedéléc, and H. P. Buchkremer, *J. Power Sources*, **195**, 1599 (2010).
26. J. C. De Vero, K. Develos-Bagarinao, H. Matsuda, H. Kishimoto, T. Ishiyama, K. Yamaji, T. Horita, and H. Yokokawa, *Solid State Ionics*, **314**, 165 (2018).
27. R. Knibbe, J. Hjelm, M. Menon, N. Pryds, M. Søgaard, H. J. Wang, and K. Neufeld, *J. Am. Ceram. Soc.*, **93**, 2877 (2010).
28. F. Wang, M. Nishi, M. E. Brito, H. Kishimoto, K. Yamaji, H. Yokokawa, and T. Horita, *J. Power Sources*, **258**, 281 (2014).
29. A. Tsoga, A. Gupta, A. Naoumidis, and P. Nikolopoulos, *Acta Mater.*, **48**, 4709 (2000).
30. A. Mai, V. Haanappel, S. Uhlenbruck, F. Tietz, and D. Stöver, *Solid State Ionics*, **176**, 1341 (2005).
31. V. Wilde, H. Störmer, J. Szász, F. Wankmüller, E. Ivers-Tiffée, and D. Gerthsen, *ECS Trans.*, **66**, 103 (2015).
32. A. Leonide, V. Sonn, A. Weber, and E. Ivers-Tiffée, *J. Electrochem. Soc.*, **155**, B36 (2008).
33. J. Hayd, L. Dieterle, U. Guntow, D. Gerthsen, and E. Ivers-Tiffée, *J. Power Sources*, **196**, 7263 (2011).
34. J. Joos, T. Carraro, A. Weber, and E. Ivers-Tiffée, *J. Power Sources*, **196**, 7302 (2011).
35. L. Blum, L. G. J. de Haart, J. Malzbender, N. Margaritis, and N. H. Menzler, *Energy Technol.*, **4**, 939 (2016).
36. B. Butz, R. Schneider, D. Gerthsen, M. Schowalter, and A. Rosenauer, *Acta Mater.*, **57**, 5480 (2009).
37. S. Linderoth, N. Bonanos, and K. Jensen, *J. Am. Ceram. Soc.*, **84**, 2652 (2001).
38. V. Sonn and E. Ivers-Tiffée, *Proc. 8th Eur. SOFC Forum*, B1005 (2008).
39. J. Szász, F. Wankmüller, V. Wilde, H. Störmer, D. Gerthsen, and E. Ivers-Tiffée, *ECS Trans.*, **66**, 79 (2015).
40. Y. Zheng, S. He, L. Ge, M. Zhou, H. Chen, and L. Guo, *Int. J. Hydrogen Energy*, **36**, 5128 (2011).
41. F. Wang, M. E. Brito, K. Yamaji, D.-H. Cho, M. Nishi, H. Kishimoto, T. Horita, and H. Yokokawa, *Solid State Ionics*, **262**, 454 (2014).
42. J. Szász, F. Wankmüller, J. Joos, V. Wilde, H. Störmer, D. Gerthsen, and E. Ivers-Tiffée, *ECS Trans.*, **77**, 27 (2017).
43. J. Szász, F. Wankmüller, V. Wilde, H. Störmer, and D. Gerthsen, *ECS Trans.*, **68**, 763 (2015).
44. H. Yokokawa, N. Sakai, T. Horita, K. Yamaji, M. E. Brito, and H. Kishimoto, *J. Alloys Compd.*, **452**, 41 (2008).
45. G. Lewis, *Solid State Ionics*, **152-153**, 567 (2002).
46. Z. Li, M. Toshiyuki, G. J. Auchterlonie, J. Zou, and D. John, *ACS Appl. Mater. Interfaces*, **3**, 2772 (2011).
47. Ö. Çelikbilek, E. Siebert, D. Jauffrès, C. L. Martin, and E. Djurado, *Electrochim. Acta*, **246**, 1248 (2017).
48. A. Müller, *PhD Thesis*, Universität Karlsruhe TH (2004).
49. K. Develos-Bagarinao, H. Yokokawa, H. Kishimoto, T. Ishiyama, K. Yamaji, and T. Horita, *J. Mater. Chem. A*, **5**, 8733 (2017).
50. T. Matsui, S. Li, H. Muroyama, K. Kishida, H. Inui, and K. Eguchi, *Solid State Ionics*, **300**, 135 (2017).
51. C. Kleinlogel and L. J. Gauckler, *Solid State Ionics*, **135**, 567 (2000).
52. S. Taub, K. Neuhaus, H.-D. Wiemhöfer, N. Ni, J. Kilner, and A. Atkinson, *Solid State Ionics*, **282**, 54 (2015).
53. A. Unemoto, A. Kaimai, K. Sato, N. Kitamura, K. Yashiro, H. Matsumoto, J. Mizusaki, K. Amezawa, and T. Kawada, *Solid State Ionics*, **181**, 868 (2010).
54. J. Labrincha, J. Frade, and F. Marques, *Solid State Ionics*, **61**, 71 (1993).
55. C. Nivot, C. Legros, B. Lesage, M. Kilo, and C. Argirusis, *Solid State Ionics*, **180**, 1040 (2009).
56. S. Braun, C. Yada, and A. Latz, *J. Phys. Chem. C*, **119**, 22281 (2015).
57. M. Mogensen and K. V. Hansen, in *Handbook of Fuel Cells*, John Wiley & Sons, Ltd, Chichester, UK (2010).